Comparison of measured and calculated x-ray and hot-electron production in short-pulse laser-solid interactions at moderate intensities

Th. Schlegel, S. Bastiani,* L. Grémillet, J.-P. Geindre, P. Audebert, and J.-C. Gauthier
Laboratoire pour l'Utilisation des Lasers Intenses, UMR No. 7605, CNRS–Ecole Polytechnique, CEA–Université Paris VI, Ecole Polytechnique, 91128 Palaiseau, France

E. Lefebvre and G. Bonnaud
CEA/DIF, DPTA, Boîte Postale 12, 91680 Bruyères-le-Châtel, France

J. Delettrez
Laboratory for Laser Energetics, University of Rochester, Rochester, New York 14623
(Received 14 December 1998)

Ultrashort pulse laser-solid interaction experiments with 4×10^{16} W/cm^2, 120 fs, 45° incidence angle, *p*-polarized pulses are theoretically analyzed with the help of $1\frac{1}{2}$-dimensional ($1\frac{1}{2}$ D) particle-in-cell (PIC) simulations. The laser impinges upon preformed plasmas with a precisely controlled density-gradient scale-length. PIC electron distribution functions are used as an input to 3D Monte Carlo simulations to interpret measured electron distributions and $K\alpha$ radiation emission. Satisfactory agreement between the experimental and simulation results is obtained for the measured absorption coefficient, the energy distribution of the back-scattered hot electrons, the hot-electron temperature in the bulk of the target, and the $K\alpha$ yield, when the preplasma scale-length is varied. [S1063-651X(99)00108-7]

PACS number(s): 52.50.Jm, 52.40.Nk, 52.65.Rr, 52.65.Pp

I. INTRODUCTION

High-intensity ultrafast lasers with chirped pulse amplification (CPA) [1] have opened a new field of study of laser matter interaction with solid targets [2,3]. Very short temporal and spatial scale plasmas are produced with highly transient and nonequilibrium properties. These plasmas have attracted attention as potential sources for ultrafast pulsed x rays in the sub-keV energy range [4–7] and in the keV range [8–10]. Experimental efforts for bringing picosecond time resolution in x-ray diffraction, spectroscopy, or microscopy of transient phenomena have been reported [11–13].

When an intense laser pulse is focused onto a solid target, a plasma is produced which is heated up to electron temperatures of hundreds of eVs, depending on the absorbed laser intensity. Thermal x rays at energies above 1 keV are produced. To get a higher x-ray radiation yield, target illumination with *p*-polarized laser light has to be used. Then, collisionless absorption processes become dominant in the laser energy deposition [14], and in their nonlinear regime, produce hot electrons, which give rise to bremsstrahlung and $K\alpha$ radiation from the target bulk. This nonthermal emission has a relatively short duration, comparable to that of the incoming laser pulse.

It is well known that the temporal shape and the contrast ratio of an intense laser pulse have a significant impact on the plasma properties [9,15]. A controlled prepulse can generate preformed plasmas with different density scale lengths. We found earlier [16] that fast electron production and nonthermal $K\alpha$ emission peak for a plasma scale length where resonant absorption is maximized [17]. In this paper we investigate the scale-length dependence of experimental observables such as the laser absorption, the electron mean energy, and the $K\alpha$ emission, by means of particle-in-cell (PIC) simulations. PIC codes have already shown their usefulness in studying, e.g., high-order harmonic generation on solids [18–20], hot-electron generation [21–24] and laser ponderomotive force effects [25,26] in the context of high intensity laser-matter interaction.

PIC codes self-consistently solve the Poisson equation and, therefore, describe the ambipolar fields generated in the collective interaction processes. They also allow one to analyze nonlinear resonance absorption, where the strong electrostatic plasma wave breaks. This wave breaking is essential for fast particle generation and cannot be treated directly in hydrodynamic simulation codes. In contrast to hydrodynamic simulations, PIC codes generally start with a preformed plasma and this can complicate the modeling of real experiments. However, in our experimental situation, the prepulse technique allows us to establish a well-controlled initial plasma state, which we use as input to our calculations.

When performing PIC simulations for various density scale-lengths, we are interested mainly in the energy distributions of fast electrons that can be computed by the code. With the help of these distributions, we can calculate the number of $K\alpha$ photons delivered as a result of laser interaction as well as the number of fast electrons escaping the plasma after being backscattered in the bulk of the target. These simulation results have been compared to the experimental data. In the following, we shall briefly describe the experimental apparatus and summarize some aspects of reso-

*Present address: Commissariat à l'Energie Atomique, DRECAM/SRSIM, Bat. 462, Centre d'Etudes de Saclay, 91191 Gif-sur-Yvette Cedex, France.

nance absorption theory relevant to our analysis. Then the results of PIC simulations will be presented. The final section will be devoted to results on hot-electron production and the conversion of their energy to hard x rays.

II. EXPERIMENTAL SETUP AND SCALE-LENGTH MEASUREMENTS

The experimental system used here has already been described in Refs. [16,17]. We recall some of its main features for the sake of clarity. The experiments were carried out with the Laboratoire d'Optique Appliquée Ti:Al_2O_3 CPA laser in Palaiseau [27]. This laser delivers 120 fs duration, 60 mJ energy, 800 nm wavelength, 10 Hz repetition rate pulses. The laser intensity contrast ratio was measured to be better than 10^{-8} (at 2 ps before the main pulse) by third order autocorrelation techniques. The main laser pulse was focused at 45° incidence angle by a 40 cm ($f/16$) focal length MgF_2 lens onto solid SiO_2 flat targets. The 20 mm diameter main laser beam is reflected on a mirror having a 6 mm diameter hole drilled in its center, which allows the transmission of a small part of the beam profile. This second beam is time-delayed with a variable delay line and, after transmission through a second apertured mirror, is superimposed on the main laser beam. The focal spot of the main beam being much smaller than the focal spot of the prepulse beam, the interaction of the main beam with the preplasma can be considered as almost one-dimensional. Typically, this system gives intensities on the target of 4×10^{16} W cm^{-2} for the main pulse and 4×10^{14} W cm^{-2} for the prepulse.

The measuring device for the suprathermal electrons is a multichannel electron spectrometer, fitted with a permanent magnetic field of ≈260 G. The detectors are six silicon surface barrier detectors, with an active thickness variable between 100 and 1000 μm. The energy range covered by this instrument extends from 20 to 200 keV. The Si $K\alpha$ emission is dispersed by means of a Von Hamos spectrograph built with a PET (pentaerythritol) crystal (2d = 8.742 Å) having a 10 cm curvature radius. The spectra are collected at an angle of 10° with respect to the target normal with a cooled (−40 °C) x-ray sensitive charge-coupled device camera [9].

For the electron density-gradient scale-length measurements, we used the technique of frequency-domain interferometry [28] that we have extended to allow simultaneous measurements of the phase shift for the two (s and p) probe polarizations. Details on this technique are given elsewhere [29,30].

The electron density-gradient scale-length measurements were interpreted with the FILM hydrocode [31]. Hydrodynamic simulations of the prepulse interaction with a solid target yield nearly exponential density profiles. The comparison of the observed scale-length values with results of the interferometric measurements shows excellent agreement. As an example, experimental results obtained after illumination of a fused silica target by a prepulse with 120 fs duration and an intensity of 4×10^{14} W/cm^2 are shown in Fig. 1 compared to FILM simulation results and to the predictions of an isothermal model [32]. This model shows that the time variation of the scale length around critical density ($n_e=1.7\times10^{21}$ cm^{-3}) is governed by the amount of energy deposited by the laser prepulse. In the following, results of Fig. 1 will be used to convert the prepulse delay into an electron density-gradient scale-length.

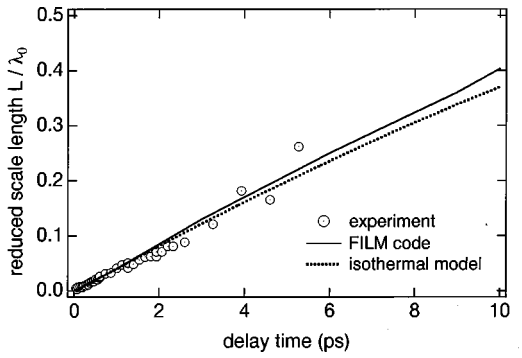

FIG. 1. Measured electron density-gradient scale length in a fused silica plasma as a function of time after the prepulse (open circles). Laser conditions are indicated in the text. The solid line is the result of a FILM simulation. The dotted line shows the isothermal expansion model with $Te=50$ eV at the peak of the laser pulse and an averaged charge $Z^*=5$.

III. COMPARISON OF EXPERIMENTAL DATA WITH ESTIMATES FROM RESONANCE ABSORPTION THEORY

For p-polarized laser pulses, the electric field component which is directed parallel to the plasma density gradient drives electrostatic oscillations. At the critical surface the local plasma frequency $\omega_p=(e^2n_e/m_e\epsilon_0)^{1/2}$ is equal to the laser frequency ω_0 and the plasma oscillations are driven resonantly. If the laser radiation is sufficiently intense, the plasma response can become nonlinear. Particle trapping and wave breaking occur, and electrons with high energies are generated. The evanescent axial field driving plasma oscillations at the critical surface can be expressed in the form [33,34]

$$E_d=cB_c\sin\theta=\frac{\Phi(\zeta)}{2\pi\sqrt{L/\lambda_0}}E_0, \tag{1}$$

where $\zeta=(2\pi L/\lambda_0)^{1/3}\sin\theta$ and $\Phi(\zeta)$ is the Denisov function, which was found by integrating the plane wave equation for a linear density profile [34]. In the above formula B_c is the magnetic field at the critical surface, θ the angle of incidence, E_0 the free-space radiation electric field amplitude, and $L=n_c/|dn/dx|_c$ the density-gradient scale length. Normalizing this scale-length to the vacuum laser wavelength, we get the dimensionless parameter L/λ_0, which will be used in the following. Assuming a small damping frequency in comparison to the frequency of the plasma oscillations, the absorbed energy flux is [35]

$$I_{abs}\approx\frac{\pi}{2}\epsilon_0\omega_0LE_d^2. \tag{2}$$

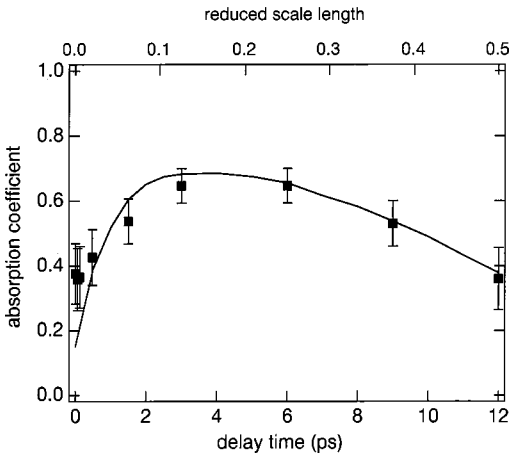

FIG. 2. Absorption coefficient estimates for different delay times and reduced scale length using Denisov's theory. Closed squares are experimental values from Ref. [17].

Using both equations we obtain the fractional absorption of the incident light wave $f_A=\Phi^2(\zeta)/2$. A rather good approximation to $\Phi(\zeta)$, obtained for a linear density profile [35], is $\Phi(\zeta)\approx 2.3\zeta \exp(-2\zeta^3/3)$. In Fig. 2, estimated absorption coefficients are plotted together with the experimental data for the corresponding scale lengths (see Fig. 2 of Ref. [17]). Both data sets show a similar behavior. The absorption peaks at approximately the same value of L/λ_0. Resonance absorption decreases at short scale length [see Eq. (2)], but vacuum heating sets in and the overall laser absorption does not go down to zero [36]. Resonance absorption is also lower for large L due to a weaker driving field amplitude after tunneling over long distances from the turning point to the critical surface. This can be deduced directly from Eq. (1) and the approximate value of $\Phi(\zeta)$ quoted above because the driving field at the critical surface decays exponentially with the scale-length.

The resonance field amplitude can be limited by different processes, namely, the nonlinear effect (wave breaking) and the effect of thermal pressure (convection). Hydrodynamic simulations using the FILM hydrocode where resonance absorption was included by means of an *ad hoc* ''collision'' frequency added to the usual one bound to inverse bremsstrahlung have shown [31] that plasma temperatures, at irradiation conditions typical for our experiments, reached a few hundreds of eV. For $T_e=600$ eV, the electron thermal velocity is $v_{te}/c=0.034$. The electron quiver velocity in the plasma wave saturated by thermal convection is $v_w \approx 1.2[(\omega_0 L)/v_{te}]^{2/3} v_d$ (where $v_d=eE_d/m_e\omega_0$ is the electron quiver velocity associated to the resonance field E_d) [37]. At the temperatures of interest for our experiments, this velocity always exceeds the cold wave-breaking velocity. Consequently, the limiting process in our case is wave breaking and not thermal convection.

IV. NUMERICAL RESULTS OF PIC SIMULATIONS

A. General description of the simulations

We have performed detailed particle-in-cell modeling of the experiments described in Ref. [17]. We used the $1\frac{1}{2}$D code EUTERPE [38] with two velocity (parallel and perpendicular to the laser axis) and one space (parallel to the laser axis) components. It calculates the relativistic motion of a large number of macroparticles in a plane *p*-polarized electromagnetic wave. Oblique incidence of the laser radiation on the plasma is treated by means of the relativistic ''boost-frame'' transformation [39]. This method reduces the computational efforts remarkably, because it transforms a 2D problem into a 1D one. To check the validity of our 1D geometry approach, we have performed a limited set of 2D simulations using the EMI2D2U PIC code [40] initialized with the present experimental conditions. For the range of electron density-gradient scale length explored ($L/\lambda_0 \leqslant 0.6$) and the moderate laser intensities that we have used, we found no evidence of parametric instabilities. Signatures of such instabilities were searched in 2D (xy) plots of the electric field and of the electron current. We checked that the variation of these observables along the y axis (parallel to the target surface) was the same as the ones obtained in 1D geometry, but plotted as a function of time. This points to the fact that, in the absence of instabilities, space along the y axis and time are equivalent, a feature which is the background of the ''boost-frame'' transformation quoted above.

In all simulations, initial temperatures of $T_e=0.6$ keV for electrons and of $T_i=0.1$ keV for ions were assumed. The particle momentum distributions were initialized to Maxwellian distributions with these temperatures. In the course of the simulations, particles reaching the high density (right) boundary of the simulation box were reinjected using the initial momentum distribution. Particles reaching the boundary on the vacuum (left-hand) side of the box were simply reflected. Only a few particles were reflected in most of the calculations because the vacuum region in front of the plasma was chosen sufficiently large [$\approx(3-4)\lambda_0$]. Exponential density profiles and maximum plasma densities in the range $(4-27)n_c$ were used in the simulations. Another important parameter is the laser pulse shape. In contrast to commonly used ramp-type pulse envelopes, we used Gaussian pulses with 120 fs full-width-at-half-maximum or $\sin^2$ pulses with the same temporal width. Pulses of both shapes carry almost the same energy but simulations with $\sin^2$ pulses need less computer time. All simulations were carried out with a fixed maximum laser intensity $I_l=4\times 10^{16}$ W/cm^2 and a wavelength $\lambda_0=800$ nm. The mass ratio M_i/Zm_e was equal to 3600.

With the help of several diagnostic routines embedded in the code, we looked for observables such as laser light absorption, energy distribution of electrons and ions inside the plasma and on the right boundary (overdense plasma), and mean energy and directionality of the electrons as a function of the initial plasma scale length. In addition to a comparison of the quantities observed in the experiments and in the simulations, a further goal of our work was to obtain a more detailed understanding of the electron acceleration processes. One of the pending questions concerned the maximum kinetic energy that the electrons can gain. In experiments, as well as in simulations, particles with kinetic energies much higher than the one deduced from the wave-breaking estimate were detected. To find an explanation for that behavior, we followed the motion of labeled electrons through the region of plasma resonance. Position, momentum, kinetic en-

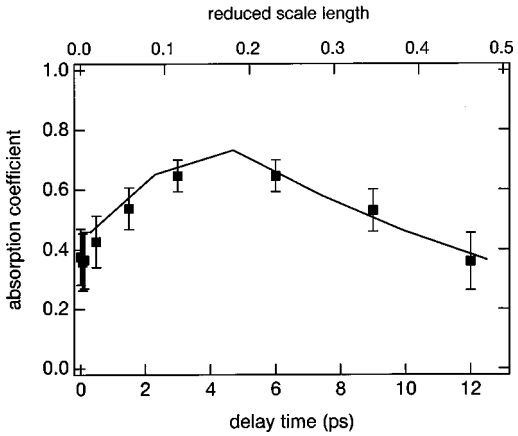

FIG. 3. Laser light absorption (solid line) of the main pulse as a function of time after the prepulse (or the reduced scale length). The squares show the values obtained experimentally.

ergy, and the electric and magnetic field components ''seen'' by these particles were stored and analyzed off-line. Density profile modifications due to thermal and ponderomotive pressures in the dense plasma were also investigated.

B. Laser absorption coefficient

We first show the simulated absorption coefficients as a function of the reduced initial scale length. In Fig. 3, the solid line was obtained with $\sin^2$ laser pulses. Absorption measured in the experiment is given by closed squares. The simulation data are in good agreement with the experiment. We reproduce the location of the absorption coefficient maximum found experimentally at $L/\lambda_0 \simeq 0.2$ as well as its value between 0.6 and 0.7.

C. Electric fields and currents

The spatiotemporal distribution of the electric field close to the peak of the laser pulse is shown in Fig. 4 in a plasma with the optimum (with respect to laser absorption) $L/\lambda_0 \simeq 0.2$. The interference pattern of the incoming and reflected longitudinal electric field E_x is clearly seen. We also plotted the critical surface at $n_e = n_c$. The field is given in units of $m_e\omega_0 c/e$, so that the picture shows the longitudinal component of the quiver velocity of an electron in the harmonic field normalized to the velocity of light. In all simulations the incident wave amplitude at maximum intensity is equal to 0.137 in these units. The time coordinate is always given in units of the laser period and the space coordinate in units of the laser wavelength λ_0. The resonance field is clearly larger than the incident field, and it extends over roughly $\lambda_0/5$ (see the regions close to the critical density surface at 46, 48, and $50T_0$ in Fig. 4). In front of the critical surface a large negative space charge field has been formed. The critical surface oscillates with the laser frequency (as also observed in Ref. [41]). This is the region where electrons gain high kinetic energies if they transit fast enough to feel only the accelerating phase of the oscillating electric field. The longitudinal electron current component is shown in Fig. 5, for the same simulation conditions as the one used in Fig. 4. Again, fol-

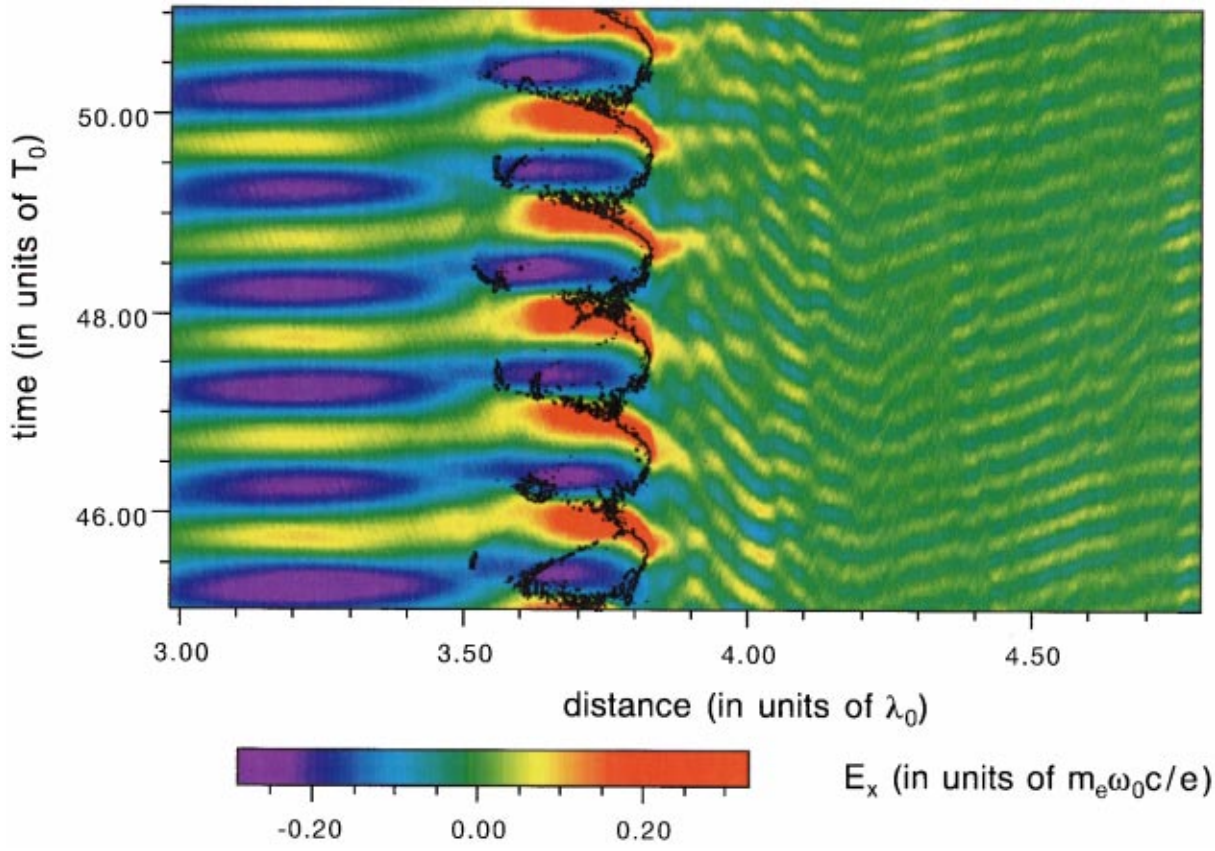

FIG. 4. (Color) Longitudinal electric field E_x in units of $m_e\omega_0 c/e$ as a function of the coordinate x (in laser wavelengths) and time (in laser periods). The critical surface is shown with black dots. The initial scale length is $L/\lambda_0 = 0.2$.

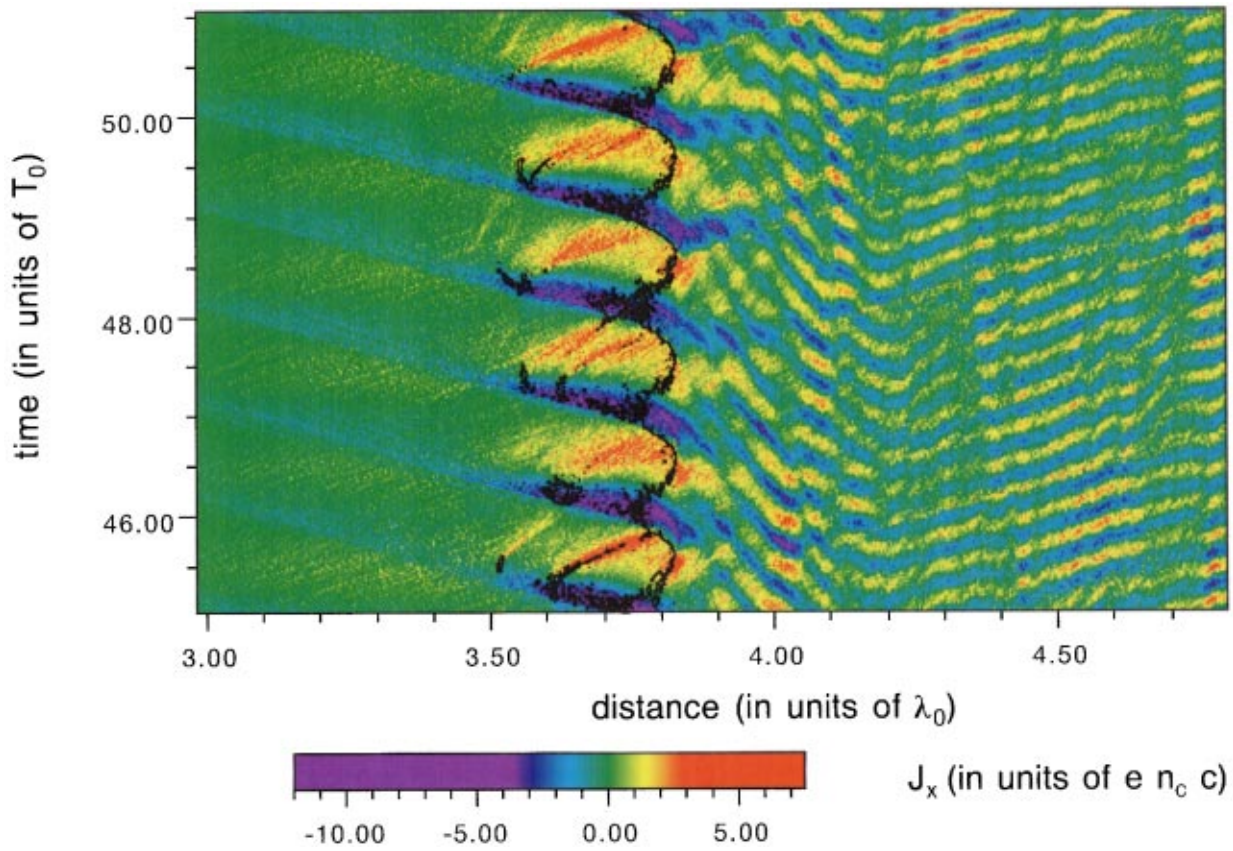

FIG. 5. (Color) Electron current J_x parallel to the target normal as a function of the coordinate x (in laser wavelengths) and time (in laser periods) from a simulation with $L/\lambda_0 = 0.2$. The critical surface is shown with black dots.

lowing the periodicity of the laser light, a large current of electrons accelerated towards vacuum is observed, as well as the corresponding return current after reflection on the space charge potential (see Fig. 5). The transverse current J_y (not shown) has also been calculated. Its magnitude illustrates the fact that a transverse momentum is transferred to the target during the absorption of obliquely incident light.

The different physical situations obtained while varying the initial scale-length are collected in Fig. 6. For three values of $L/\lambda_0 = 0.01$, 0.2, and 0.6 the longitudinal electric field

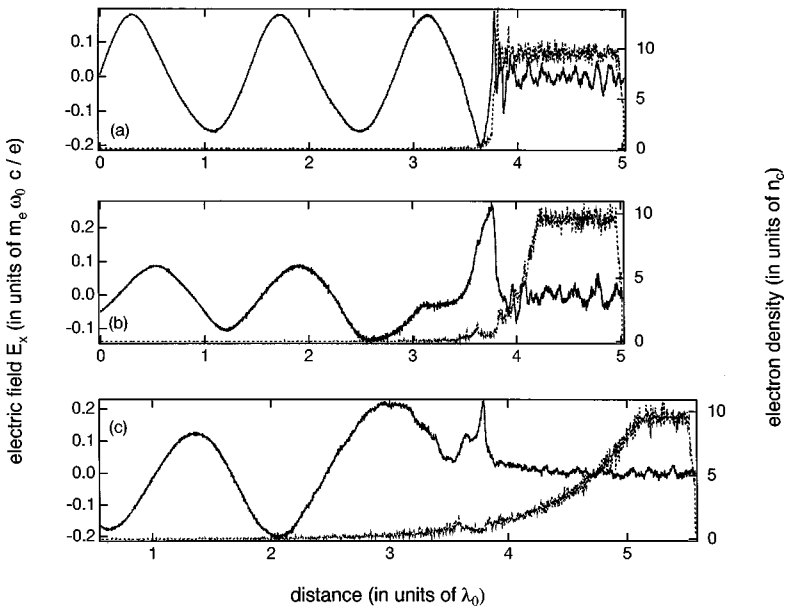

FIG. 6. Longitudinal electric field (solid line) and electron density profiles (dotted line) for three different initial gradient scale lengths: (a) $L/\lambda_0 = 0.01$, (b) $L/\lambda_0 = 0.2$, and (c) $L/\lambda_0 = 0.6$.

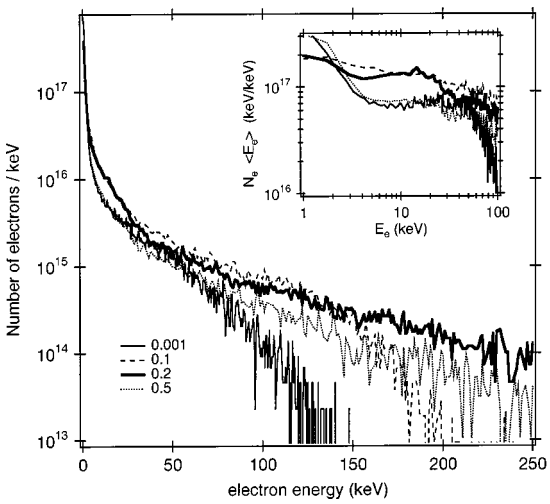

FIG. 7. Number of electrons flowing through the right (overdense) edge of the simulation box, per keV and per cm^2 of target surface, as a function of kinetic energy for several values of the initial scale length. The inset shows the distribution of the electron energies as a function of electron energy.

E_x (solid lines) is shown at the time where the resonance field is close to its maximum. We see a large resonance for $L/\lambda_0 = 0.2$ after the field has tunneled from the turning point to the critical point. Since the distance between these two points increased in the case of $L/\lambda_0 = 0.6$ the resonance becomes weaker, as expected. In the overcritical plasma, strong electrostatic field perturbations with the frequency of the plasma wave can be observed. These disturbances are caused by the jets of energetic electrons flowing in the bulk of the target (see Fig. 5). From the existence of similar perturbations in the transverse field pattern inside the target, we can conclude that a strong directionality of the fast electron jets occurs. This was already observed in previous 2D simulations performed in the context of the interaction of a short pulse laser field with a corrugated solid target [42]. We will see below that the oscillations excited by the leading edge of an electron bunch may in turn influence the motion of electrons arriving later during the same laser cycle. In addition to the field distribution, the electron density profile is also shown in Fig. 6. When the scale length is increased, an undercritical plasma shelf develops, expands, and eventually becomes overcritical somewhere in front of the critical surface. At the same time, the plasma profile is steepened on the dense plasma side. This results from the well-known action of the ponderomotive force of the resonant field.

D. Electron distribution functions

A rather informative diagnostic in PIC simulations is the energy distribution functions of the particles. For example, one can count all the electrons reaching the right boundary of the simulation box and ''measure'' their energy before reinjecting them with thermal velocities. The number of electrons reaching the right edge of the system is plotted in Fig. 7, per keV and per cm^2 of target surface, as a function of energy, for several scale lengths. Looking at the inset in Fig. 7, we distinguish three different energy ranges. At very low energy, less than 1 keV, we have thermal electrons characterized by their initial temperature $T_e = 600$ eV. Then, there appears a local plateau of electrons with energies $E \approx (5-40)$ keV and a high-energy tail of the distribution function follows. This tail is rather noisy but this cannot be avoided in PIC simulations because they use a relatively small number of particles. As already mentioned above, additional fluctuations can be produced by interaction of the fast electrons with the electron-excited plasma oscillations in the overdense target.

Now we try to understand how electrons can gain energies of some hundred keV at laser intensities in the mid-10^{16} W/cm^2 range (i.e., quiver electron energies of a few keV). As already mentioned, experiments and simulations give maximum energies which are far above the values given by simple estimates. We followed some ''test'' electrons during their interaction with the laser and the laser-driven plasma waves. In Fig. 8 the trajectory of one such electron is plotted in the electric field E_x. The motion of the particles in the resonance region is strongly dependent on their ''phase matching'' with the plasma wave. The figure contains, besides the electric field, time-history plots of the kinetic energy of the test particle, together with the electron density it ''sees'' during its trajectory. In Fig. 8, the electron starts with thermal energy at the entrance of the resonant field, becomes trapped in the plasma wave and is accelerated to an energy of the order of 100 keV. The electron makes a large excursion in front of the target during the next two laser cycles. This behavior has been described as the formation of ''cloud electrons'' which do not return to the target bulk during the same laser cycle where they originated [21,43,44]. On its way back to the target, the test electron arrives at the critical surface just in phase with the negative half-period of the resonance field, and gets an additional ''kick'' of more than 50 keV. Slightly decelerated by the resonance of the next cycle, its velocity is increased again in the plasma wave field (seen as undulations in the target bulk in Fig. 8) up to 200 keV. Continuing its motion in the bulk of the target, part of this energy is converted into electrostatic energy of the dense plasma oscillations. Only a relatively small number of electrons will have the right ''phase'' with respect to the resonant field to be accelerated to such large energies, a very much larger number of electrons will be resonantly heated to energies in the range between 10 and 40 keV (see Fig. 7).

E. Coupling with the Monte Carlo code

In this section, we present some results on electron backscattering and $K\alpha$ production, modeled with a 3D Monte Carlo code. This code, named PROPEL, is a relativistic extension of the one that we developed in our previous studies [9]. We used stopping power and opacity data corresponding to the SiO_2 targets shot in the experiments. Our goal is to interpret the experimental data obtained with the electron spectrometer [17], which was looking at those electrons escaping the ambipolar field in front of the target. With PROPEL, we first simulated monoenergetic electron beams injected perpendicular to the target surface, and looked for the energy distribution of backscattered electrons. Then, we weighted each of these distributions with the number of electrons per

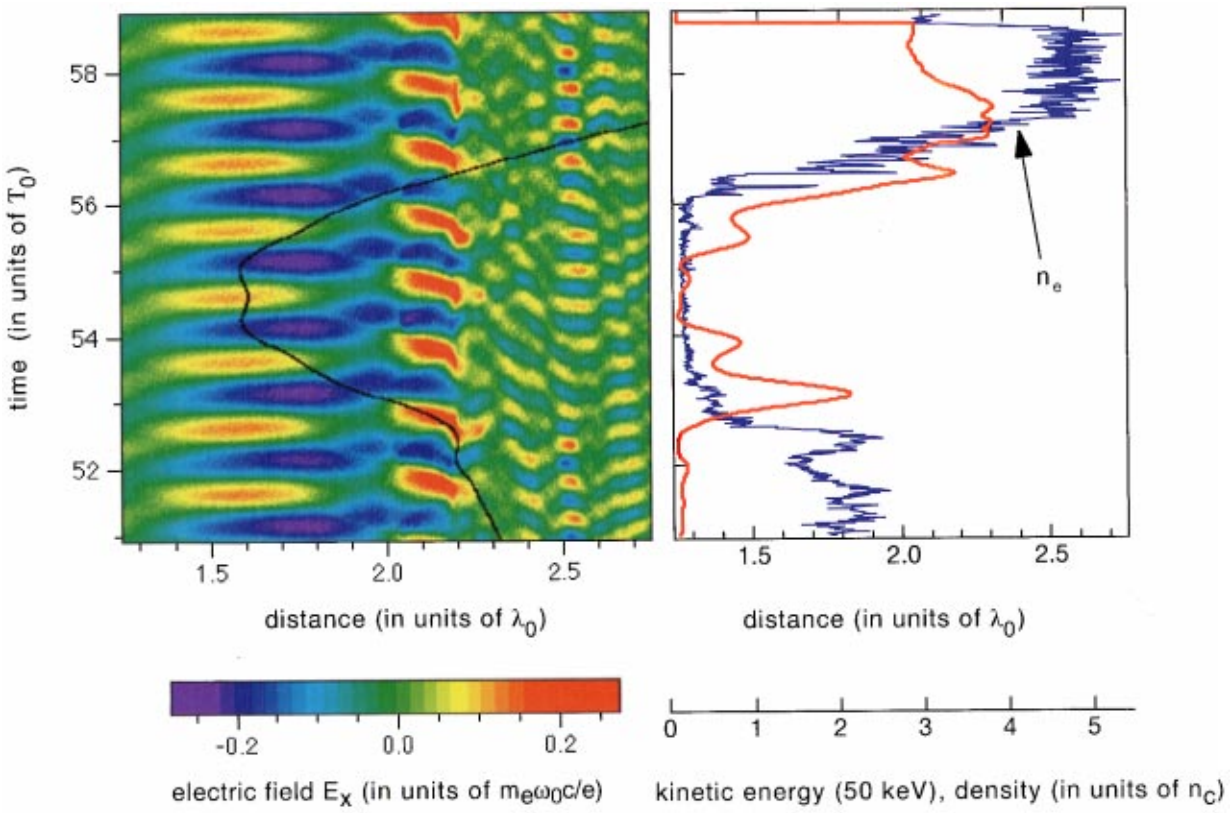

FIG. 8. (Color) Trajectory of a test electron as a function of space in wavelength units and as a function of time in laser periods. The longitudinal electric field is superimposed. On the right, the electron density (thin solid line) and the kinetic energy (heavy solid line) of this test particle are shown with its trajectory. The reduced initial scale length was $L/\lambda_0 = 0.2$.

energy bin calculated by the PIC code. Results for three different scale lengths are shown in Fig. 9 and can be directly compared to the results from the electron spectrometer. We would like to stress the point that there is *no adjustable parameter in this absolute comparison*. For rather steep density profiles of the preformed plasma and for the case of more extended plasmas ($L/\lambda_0 > 0.3$) we find a good agreement of our simulated electron distributions with those observed experimentally, in the energy range above 70 keV. A different picture follows for the case of optimum resonance ($L/\lambda_0 \approx 0.2$). Here, the experimental hot temperature (the slope of the electron energy distribution) is larger than in the simulations. In the energy range below 50–70 keV, we obtain marked differences between experimental and simulation results, independently of the scale-length.

Our theoretical model overestimates the number of electrons in this energy region, especially for plasmas with initially steep density profiles. What one cannot understand on the basis of these simulations are the deviations between experiment and theory for $L/\lambda_0 \approx 0.2$ when resonance absorption is an important phenomenon. A possible hint can be obtained from the strong plasma waves observed in the overcritical plasma. Discussing above the interaction of test electrons with electric fields, we have seen that the fastest particles lose part of their energy to these waves. On the other side, slower electrons can gain some energy there. If these processes are overestimated in our PIC simulations, we will end up with electron distributions colder than the real ones.

Another reason, which can be responsible for the observed differences between the theoretical model and the results from the electron spectrometer, may be related to the interaction geometry. We have previously shown that high energy electrons are prone to penetrate in the target at much larger radial positions than low energy electrons [9]. Accordingly, low energy electrons are more sensitive to electrostatic fields that may appear at the target surface. A comparison with 2D PIC simulations has shown that the charge separation field in a 2D geometry is smaller than in 1D. As a consequence, low energy electrons which return to the target close to the center of the focal spot could be more affected by these fields. Another difference in the behavior of high and low energy electrons can be found in transport inhibition effects. Recent papers [45] have shown that the electrical conductivity plays a significant role in fast electron energy deposition. An electric field builds up at the surface of the target which limits the electron penetration. Accordingly, the post-processing of electron distributions by the Monte Carlo code has to be regarded as rather indicative.

Using the Monte Carlo code, results on the emission of $K\alpha$ photons following the removal of a K-shell electron can also be obtained. The code takes into account the opacity of the material located between the point of emission and the point of observation, at any angle with respect to the normal of the target. The knowledge of the $K\alpha$ output for a chosen material given in numbers of photons per electron delivered in one steradian allows us to calculate the absolute number

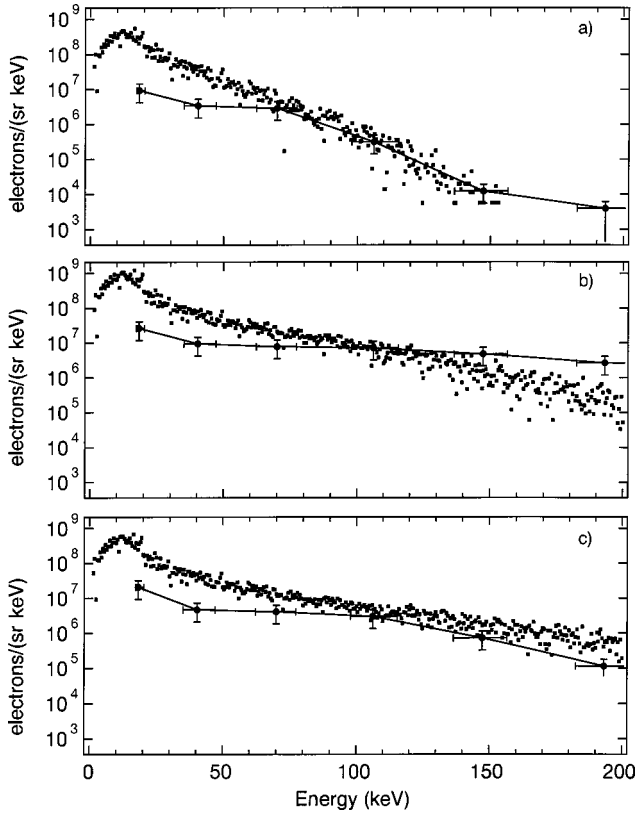

FIG. 9. Absolute electron distributions after backscattering from the target, modeled with the Monte Carlo code PROPEL coupled to the PIC code EUTERPE. The corresponding experimental results are shown with error bars. (a) $L/\lambda_0 = 0.001$, (b) $L/\lambda_0 = 0.2$, and (c) $L/\lambda_0 = 0.5$.

of produced $K\alpha$ x-ray photons. To get the integral photon number per steradian we have to convolve the $K\alpha$ yield with the electron distributions shown in Fig. 7. The calculated $K\alpha$ photon numbers for several values of the initial scale-length together with calibrated measurements [46] are given in Fig. 10. These results are normalized to 1 J of incident laser energy. We stress again that this comparison is absolute. We observe a peak of emission which is strongly displaced with respect to the experimentally determined one. Because of the sharp energy threshold behavior of the $K\alpha$ yield function around 15 keV, we immediately understand the difficulty to get a reasonable result for integral photon numbers in plasmas with steep profiles in the framework of our theoretical model. Since the PIC modeling strongly overestimates the energy distribution functions in the ''low'' energy part, we will not get the experimentally observed optimum in $K\alpha$ at prepulse delays around 6 ps.

V. CONCLUSION

In summary, we have investigated theoretically the interaction of short intense laser pulses at oblique incidence and *p* polarization with preformed plasmas. A $1\frac{1}{2}$D PIC code implementing the ''boost-frame'' technique was used to simulate laser energy conversion to fast electrons. The initial conditions were chosen to be as close as possible to the experimental situation. With additional 2D simulations, we

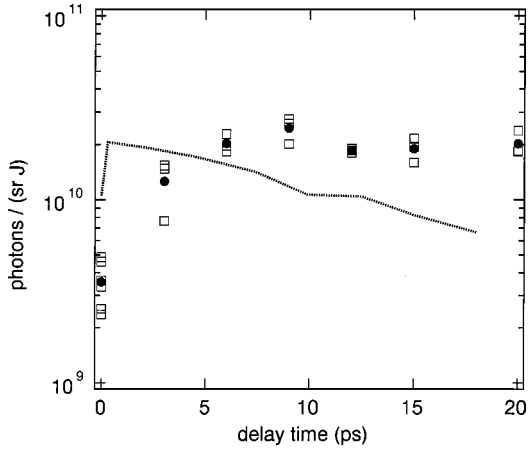

FIG. 10. Simulated $K\alpha$ photon yield (dotted line) as a function of the delay time together with experimental values in SiO_2. Open squares are the results of individual measurements, and the dots are the mean values.

confirmed our assumption that the electron heating is dominated by the anomalous skin effect and resonance absorption but not by plasmas instabilities. The observed absorption coefficients as a function of the prepulse delay agree with the experimental results.

This kinetic model allowed us to explore the rather complex picture of hot-electron production in more detail. We observed the energy distribution functions of energetic particles in plasmas of different scale lengths. In the range of optimum resonance absorption, these distributions exhibit a large number of electrons with a mean energy around 12 keV and a high temperature tail. By post-processing the particle-in-cell results with Monte Carlo simulations, we looked for the changes in the electron distributions due to electron-ion collisions and compared the results to the experimental observations. Data in the high energy range (above 70 keV) are in good agreement independently of the preformed plasma state except for the case of optimized resonance absorption. Some possible explanations for the observed differences have been discussed. Using the Monte Carlo model, and the PIC electron distributions, the integral $K\alpha$ photon numbers produced in the SiO_2 target, per steradian per unit laser energy were determined. A qualitative agreement with the calibrated experimental values was achieved for plasmas with a prepulse delay exceeding 4–5 ps. The maximum number of experimentally measured photons of approximately 3×10^{10} photons/sr J could be reproduced theoretically.

ACKNOWLEDGMENTS

We gratefully acknowledge the support of the laser staff at LOA where the experiments were carried out. We deeply thank A Héron, J.-C. Adam, and G. Laval for their kindness in providing the results of the 2D simulations. This work was supported by the Centre National de la Recherche Scientifique, the Commissariat à l'Energie Atomique, and the European Community under Large Scale Facilities Contract No. CHGE-CT93-0021, Human Capital and Mobility Contract No. CHRX-CT93-0338, and Training and Mobility Contract No. ERBFMRXCT96-0080.

[1] M. D. Perry and G. Mourou, Science **264**, 917 (1994).
[2] J.-C. Gauthier, in *Laser Interaction with Matter*, IOP Conference Series Vol. 140, edited by S. Rose (IOP, Bristol, 1994), p. 1.
[3] P. Gibbon and E. Förster, Plasma Phys. Controlled Fusion **38**, 769 (1996).
[4] J. F. Pelletier, M. Chaker, and J.-C. Kieffer, Opt. Lett. **21**, 1040 (1996).
[5] J. F. Pelletier, M. Chaker, and J.-C. Kieffer, Appl. Phys. Lett. **69**, 2172 (1996).
[6] J. Workman, A. Maksimchuk, X. Liu, U. Ellenberger, J. S. Coe, X.-Y. Chien, and D. Umstadter, J. Opt. Soc. Am. B **13**, 125 (1996).
[7] M. S. Dzhidzhoev, V. M. Gordienko, V. V. Kolchin, S. A. Magnitsky, V. T. Platonenko, A. B. Savel'ev, and A. P. Tarasevitch, J. Opt. Soc. Am. B **13**, 143 (1996).
[8] J.-C. Kieffer, M. Chaker, J.-P. Matte, H. Pépin, C. Y. Côté, Y. Beaudoin, C. Y. Chien, S. Coe, G. Mourou, and O. Peyrusse, Phys. Fluids B **5**, 2676 (1993).
[9] A. Rousse, P. Audebert, J. P. Geindre, F. Falliès, J.-C. Gauthier, A. Mysyrowicz, G. Grillon, and A. Antonetti, Phys. Rev. E **50**, 2200 (1994).
[10] J.-C. Kieffer, Z. Jiang, A. Ikhlef, and C. Y. Côté, J. Opt. Soc. Am. B **13**, 132 (1996).
[11] A. Rousse, P. Audebert, J.-P. Geindre, F. Falliès, J.-C. Gauthier, A. Mysyrowicz, A. Dos Santos, G. Grillon, and A. Antonetti, J. Phys. B **27**, L697 (1994).
[12] F. Ráksi, K. R. Wilson, Z. Jiang, A. Ikhlef, C. Y. Côté, and J.-C. Kieffer, J. Chem. Phys. **104**, 6066 (1996).
[13] C. Rischel, A. Rousse, I. Uschmann, P. A. Albouy, J.-P. Geindre, P. Audebert, J.-C. Gauthier, E. Förster, J.-L. Martin, and A. Antonetti, Nature (London) **390**, 490 (1997).
[14] A. A. Andreev, K. Yu. Platonov, and J.-C. Gauthier, Phys. Rev. E **58**, 2424 (1998).
[15] C. Y. Côté, J.-C. Kieffer, and O. Peyrusse, Phys. Rev. E **56**, 992 (1997).
[16] J.-C. Gauthier, S. Bastiani, P. Audebert, J.-P. Geindre, A. Rousse, C. Quoix, G. Grillon, A. Mysyrowicz, A. Antonetti, R. Mancini, and A. Shlyaptseva, Proc. SPIE **3157**, 52 (1997).
[17] S. Bastiani, A. Rousse, J.-P. Geindre, P. Audebert, C. Quoix, G. Hamoniaux, A. Antonetti, and J.-C. Gauthier, Phys. Rev. E **56**, 7179 (1997).
[18] P. Gibbon, Phys. Rev. Lett. **76**, 50 (1996).
[19] P. A. Norreys, M. Zepf, S. Motsaizis, A. P. Fews, J. Zhang, P. Lee, M. Bakarezos, C. N. Danson, A. Dyson, P. Gibbon, P. Loukakos, D. Neely, F. N. Walsh, and J. S. Wark, Phys. Rev. Lett. **76**, 1832 (1996).
[20] R. Lichters, J. Meyer-ter-Vehn, and A. Pukhov, Phys. Plasmas **3**, 3425 (1996).
[21] P. Gibbon, Phys. Rev. Lett. **73**, 664 (1994).
[22] E. Lefebvre and G. Bonnaud, Phys. Rev. E **55**, 1011 (1997).
[23] F. N. Beg, A. R. Bell, A. E. Dangor, C. N. Danson, A. P. Fews, M. E. Glinsky, B. A. Hammel, P. Lee, P. A. Norreys, and M. Tatarakis, Phys. Plasmas **4**, 447 (1997).
[24] M. H. Key, M. D. Cable, T. E. Cowan, K. G. Estabrook, B. A. Hammel, S. P. Hatchett, E. A. Henry, D. E. Hinkel, J. D. Kilkenny, J. A. Koch, W. L. Kruer, A. B. Langdon, B. F. Lasinski, R. W. Lee, B. J. MacGowan, A. MacKinnon, J. D. Moody, M. J. Moran, A. A. Offenberger, D. M. Pennington, M. D. Perry, T. J. Phillips, T. C. Sangster, M. S. Singh, M. A. Stoyer, M. Tabak, G. L. Tietbohl, M. Tsukamoto, K. Wharton, and S. C. Wilks, Phys. Plasmas **5**, 1966 (1998).
[25] S. C. Wilks, W. L. Kruer, M. Tabak, and A. B. Langdon, Phys. Rev. Lett. **69**, 1383 (1992).
[26] J. Denavit, Phys. Rev. Lett. **69**, 3052 (1992).
[27] C. Le Blanc, G. Grillon, J.-P. Chambaret, A. Migus, and A. Antonetti, Opt. Lett. **18**, 140 (1993).
[28] P. Blanc, P. Audebert, F. Falliès, J.-P. Geindre, J.-C. Gauthier, A. Dos Santos, A. Mysyrowicz, and A. Antonetti, J. Opt. Soc. Am. B **13**, 118 (1996).
[29] J. P. Geindre, P. Audebert, A. Rousse, F. Falliès, J.-C. Gauthier, A. Mysyrowicz, A. Dos Santos, G. Hamoniaux, and A. Antonetti, Opt. Lett. **19**, 1997 (1994).
[30] L. Lepetit, G. Chériaux, and M. Joffre, J. Opt. Soc. Am. B **12**, 2467 (1995).
[31] U. Teubner, P. Gibbon, E. Förster, F. Falliès, P. Audebert, J.-P. Geindre, and J.-C. Gauthier, Phys. Plasmas **3**, 2679 (1996).
[32] M. D. Rosen, Proc. SPIE **1229**, 160 (1990).
[33] V. L. Ginzburg, *The Properties of Electromagnetic Waves in Plasmas* (Pergamon, New York, 1964).
[34] N. G. Denisov, Zh. Éksp. Teor. Fiz. **31**, 609 (1956) [Sov. Phys. JETP **4**, 544 (1957)].
[35] W. L. Kruer, *The Physics of Laser Plasma Interactions* (Addison-Wesley, Redwood City, CA, 1988).
[36] F. Brunel, Phys. Rev. Lett. **59**, 52 (1987).
[37] K. G. Estabrook, E. J. Valeo, and W. L. Kruer, Phys. Fluids **18**, 1151 (1975).
[38] G. Bonnaud and G. Reisse, Nucl. Fusion **26**, 633 (1986); E. Lefebvre, Ph.D. thesis, Université de Paris XI–Orsay, 1996 (unpublished).
[39] A. Bourdier, Phys. Fluids **26**, 1804 (1983); P. Gibbon, A. Andreev, E. Lefebvre, G. Bonnaud, H. Ruhl, J. Delettrez, and A. R. Bell, Phys. Plasmas **6**, 947 (1999).
[40] A. Héron, thèse de doctorat d'état, 1986 (unpublished).
[41] R. Lichters and J. Meyer-ter-Vehn, in *Multiphoton Processes 96* (IOP, Bristol, 1997), p. 221; R. Lichters, Ph.D. thesis, Technical University München, 1997 (unpublished).
[42] J.-C. Gauthier, S. Bastiani, P. Audebert, J.-P. Geindre, K. Neuman, T. Donnelly, M. Hoffer, R. W. Falcone, R. Shepherd, D. Price, and B. White, Proc. SPIE **2523**, 242 (1995).
[43] G. Bonnaud, P. Gibbon, J. Kindel, and E. Williams, Laser Part. Beams **9**, 339 (1991).
[44] Wei Yu, M. Y. Yu, Z. M. Sheng, and J. Zhang, Phys. Rev. E **58**, 2456 (1998).
[45] M. E. Glinsky, Phys. Plasmas **2**, 2796 (1995); A. R. Bell, J. R. Davies, S. Guérin, and H. Ruhl, Plasma Phys. Controlled Fusion **39**, 653 (1997).
[46] J.-C. Gauthier, J.-P. Geindre, P. Audebert, S. Bastiani, Th. Schlegel, C. Quoix, A. Rousse, and A. Antonetti, in *11th Topical APS Conference on Atomic Processes in Plasmas*, edited by Eugene Oks and Michael S. Pindzola, AIP Conf. Proc. No. 443 (AIP, New York, 1998), p. 92.